

# Global Tracking and Quantification of Oil and Gas Methane Emissions from Recurrent Sentinel-2 Imagery

Thibaud Ehret,<sup>\*,†</sup> Aurélien De Truchis,<sup>‡</sup> Matthieu Mazzolini,<sup>‡</sup> Jean-Michel Morel,<sup>†</sup> Alexandre d'Aspremont,<sup>¶</sup> Thomas Lauvaux,<sup>§</sup> Riley Duren,<sup>||</sup> Daniel Cusworth,<sup>⊥</sup> and Gabriele Facciolo<sup>†</sup>

<sup>†</sup>*Université Paris-Saclay, CNRS, ENS Paris-Saclay, Centre Borelli, France*

<sup>‡</sup>*Kayrros SAS, France*

<sup>¶</sup>*CNRS, Ecole Normale Supérieure, Paris and Kayrros SAS, France*

<sup>§</sup>*Laboratoire des Sciences du Climat et de l'Environnement, CEA, CNRS, UVSQ/IPSL*

<sup>||</sup>*University of Arizona, Office of Research, Innovation and Impact, Tucson, AZ, USA and Carbon Mapper, San Francisco, CA, USA*

<sup>⊥</sup>*Jet Propulsion Laboratory, California Institute of Technology, Pasadena, CA, USA*

E-mail: [thibaud.ehret@ens-paris-saclay.fr](mailto:thibaud.ehret@ens-paris-saclay.fr)

## Abstract

Methane ( $\text{CH}_4$ ) emissions estimates from top-down studies over oil and gas basins have revealed systematic under-estimation of  $\text{CH}_4$  emissions in current national inventories. Sparse but extremely large amounts of  $\text{CH}_4$  from oil and gas production activities have been detected across the globe, resulting in a significant increase of the overall O&G contribution. However, attribution to specific facilities remains a major challenge unless high-resolution images provide the sufficient granularity within O&G

basin. In this paper, we monitor known oil-and-gas infrastructures across the globe using recurrent *Sentinel-2* imagery to detect and quantify more than 800 CH<sub>4</sub> emissions. In combination with emissions estimates from airborne and *Sentinel-5P* measurements, we demonstrate the robustness of the fit to a power law from 0.1 t<sub>CH<sub>4</sub></sub>/hr to 600 t<sub>CH<sub>4</sub></sub>/hr. We conclude here that the prevalence of ultra-emitters (> 25t<sub>CH<sub>4</sub></sub>/hr) detected globally by *Sentinel-5P* directly relates to emission occurrences below its detection threshold. Similar power law coefficients arise from several major oil and gas producers but noticeable differences in emissions magnitudes suggest large differences in maintenance practices and infrastructures across countries.

## Introduction

The detection of large and frequent methane (CH<sub>4</sub>) emissions linked to oil and gas production has raised concerns in the ability of natural gas to effectively reduce greenhouse gas (GHG) emissions as a substitute to coal.<sup>1-8</sup> Over a 20-year horizon, a CH<sub>4</sub> molecule has a global warming potential close to 90 times larger than carbon dioxide (CO<sub>2</sub>).<sup>9</sup> A large part of the CH<sub>4</sub> emissions could be controlled or avoided, as they come primarily from maintenance operations at oil rigs, pipelines, or well pads, and from equipment failures.<sup>10</sup>

In order to detect and quantify GHG fossil fuel emissions produced by human activities, several satellites have been placed in orbit over the past ten years (e.g. GOSAT, OCO-2, TROPOMI), allowing a persistent monitoring of carbon dioxide and methane emissions. The *Sentinel-5P* (TROPOMI) satellite mission<sup>11</sup> provides hyper-spectral images in the short-wave infrared (SWIR) spectrum for which CH<sub>4</sub> has a significant absorption coefficient. It provides daily CH<sub>4</sub> column mole fractions over the whole globe at moderate resolutions (5-7 km) revealing multiple individual cases of unintended very large emissions (e.g. Pandey *et al.*<sup>12</sup>) and regional basin-wide anomalies.<sup>13,14</sup> However, due to its relatively low spatial resolution and moderate instrument precision, this mission remains inadequate to observe small emissions (< 25 t<sub>CH<sub>4</sub></sub>/hr) or to attribute emissions to specific facilities in densely-equipped

oil and gas basins Lauvaux *et al.*<sup>15</sup>

High resolution hyper-spectral satellite imagery from PRISMA<sup>16</sup> and GHGSat<sup>17</sup> offers much lower emission detection thresholds (0.1 to 0.2  $t_{CH_4}/hr$ ) and the capacity to attribute precisely an emission to a specific oil and gas asset. However, the tasking nature and relatively small fields of view of these products limit their viability for persistent monitoring at a global scale. Airborne campaigns,<sup>18</sup> while having an even higher spatial resolution and lower detection limits (about 0.01  $t_{CH_4}/h$ ), suffer from the same limited spatial coverage. The *Sentinel-2* mission provides persistent multi-spectral imagery in the SWIR range and with a relatively low revisit time. Although these instruments are not designed with methane detection in mind, it turns out that some of the bands are sensitive to its presence, thus enabling detection and quantification of moderate  $CH_4$  emissions. It was shown by Varon *et al.*<sup>19</sup> that combining adequately multiple SWIR bands increases the contrast of the plumes, and that having access to a reference image (at another date) without a  $CH_4$  anomaly still improves this contrast.

In this work, we applied our detection framework for large scale detection, quantification and uncertainty estimation of methane plumes using imagery coming from existing SWIR instruments onboard the *Sentinel-2* and *Landsat-8* satellites. The methodology (presented in Appendix A and B) was used to monitor oil and gas infrastructure in four countries. This led us to detect about 800 events, a dataset that we are making publicly available. We combined our measurements with data from other instruments, presented by Lauvaux *et al.*,<sup>15</sup> more adapted to detect larger emissions (*Sentinel-5P*), as well as smaller events detected with airborne campaigns. Using this combination of observed emissions, we were able to construct a robust emission power law model that has been recently proposed, which shows that global observations of ultra-emitters ( $> 25 t_{CH_4}/hr$ ) serves as an indicator for the magnitude of many more unobserved events. We also clustered the emissions based on their location, *i.e.* by country, or by date to have a better understanding of local behaviors and derive trends.

## Results

We monitored about 7000 geographical sites of interest linked to oil and gas facilities during a period of 43 months, from November 2017 to June 2021. Every site is associated to a 10x10km tile. For every tile, a time series of at least six months was extracted. In total for this study, more than 1248621 (potentially cloudy) tiles were processed over 562652 km<sup>2</sup>. The proposed dataset comprised all the manually annotated masks (see Appendix B for a complete description of the practical pipeline that was used) corresponding to the detected methane plumes at each of these locations. Each detected plume in the dataset is quantified using the IME method (See Appendix B). Fig. 1 shows a selection of methane plumes from the proposed dataset. We also associate to each plume the corresponding wind data from ECMWF-ERA5<sup>20</sup> that is used to quantify the emission. Table 1 recapitulates the data available for each emission in the database. As of May 2021, 792 plumes were detected using *Sentinel-2* images from 86 different sites of interest, mostly located in three countries: Algeria, the United States and Turkmenistan (see Fig. 3). Table 2 shows the number of detected events per country.

We then classified these emissions into two main categories: recurrent and unique. An event is said to be recurrent when at least two methane plumes have been detected in the time series of a given AOI. The rest of the emission are characterized as unique *i.e.* only one plume was detected in the considered AOI in the entire time series. We found that 58% of these plumes could be attributed to recurrent events. This means that these events are likely not due to an unexpected major incident, and could probably be avoided with a better monitoring and maintenance of oil and gas facilities. We present a more detailed histogram of recurrence of emissions in Fig. 2.

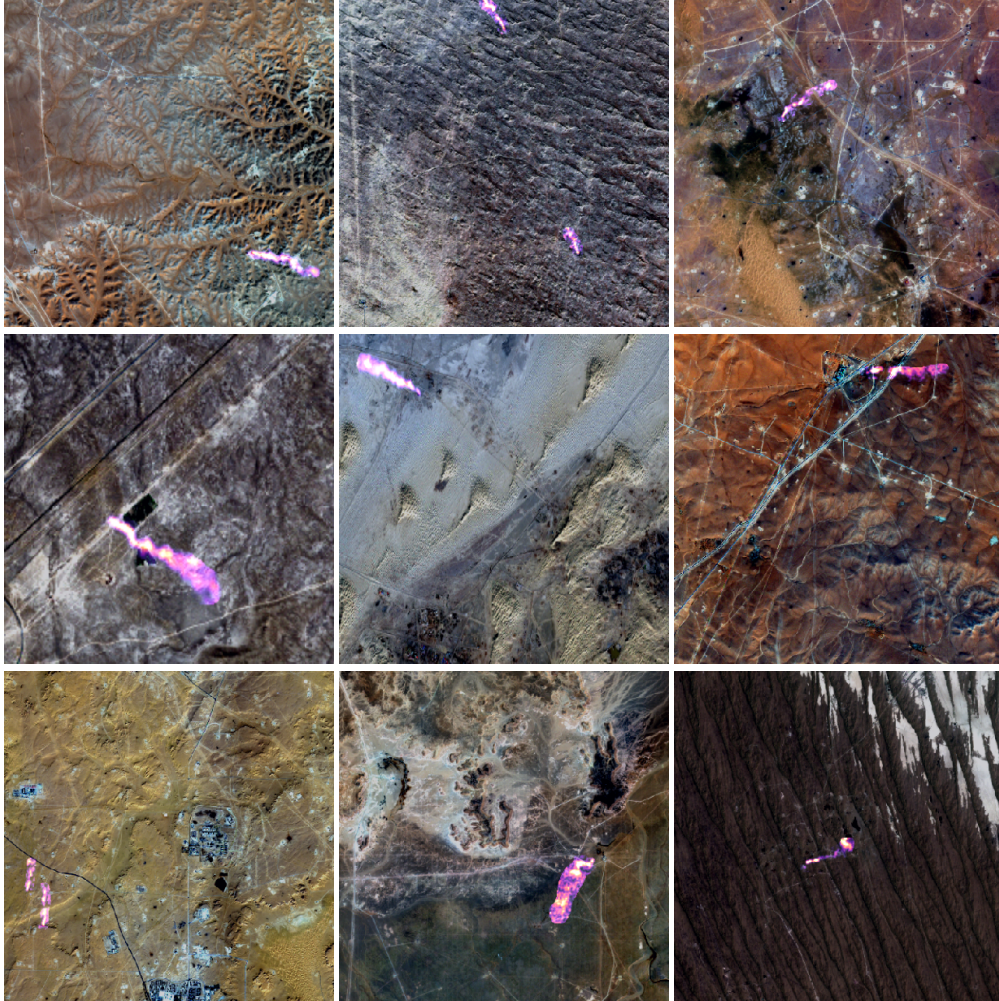


Figure 1: Examples of detected plumes over oil and gas facilities. The plume is shown as a white and purple mask (not scaled here) over the corresponding *Sentinel-2* satellite images.

## Power law fitting

In a recent paper, Lauvaux *et al.*<sup>15</sup> postulated that the emission events follow a power law distribution. This was observed using emission rates estimated from *Sentinel-5P* and airborne hyperspectral measurements. In this work, we merged the events from our *Sentinel-2* based dataset into the previously proposed power law plot<sup>15</sup> to complete the picture. The power law that we obtained is shown in Fig. 4. Note that we rescaled counts for *Sentinel-2* and airborne campaigns so that counts match for all sources for emissions rates where events can be detected by multiple sources. In practice, this means that *Sentinel-2* counts are scaled to match *Sentinel-5P* counts at  $50 \text{ t}_{\text{CH}_4}/\text{hr}$  (i.e so the regression lines intersect), while

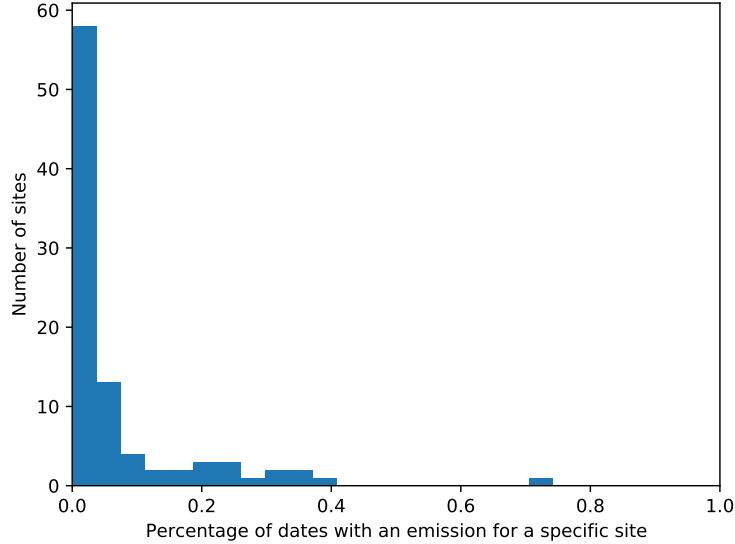


Figure 2: Histogram of recurrence of emissions.

Table 1: Data available for each emission in the plume database

Attribute	Description
long, lat	Longitude and Latitude of the source of the plume
date	Date of the event
plume_shape	Contour of the binary mask of the plume in WSG84 coordinates
u,v	Wind direction along the U and V components (in $\text{ms}^{-1}$ )
ws	Wind speed retained for the IME (the norm of (u,v))
Q	Emission rate

California<sup>2</sup> and Permian<sup>8</sup> counts are scaled to match S2 counts at  $5 \text{ t}_{\text{CH}_4}/\text{hr}$ . The rationale behind this scaling is that, everything else being equal, detection counts should match for all sources for which emission rates are above the detection limit. The scaling is thus meant to compensate for differences in spatial coverage, revisit frequency, weather impact, etc. We define the detection limit as the threshold that represents the regime in which, excepted in the most adversarial conditions, sources should be detected. In practice, it corresponds to the point below which the linear models isn't valid anymore since detections are missed. This phenomenon is visible in Fig. 4 where each curve "tails off" on the lower end. This also means that it is possible to detect emissions smaller than this limit when conditions are optimal (e.g appropriate wind conditions and good surface reflectance).

Remark that *Sentinel-2* observations are well aligned with the *Sentinel-5P* power law

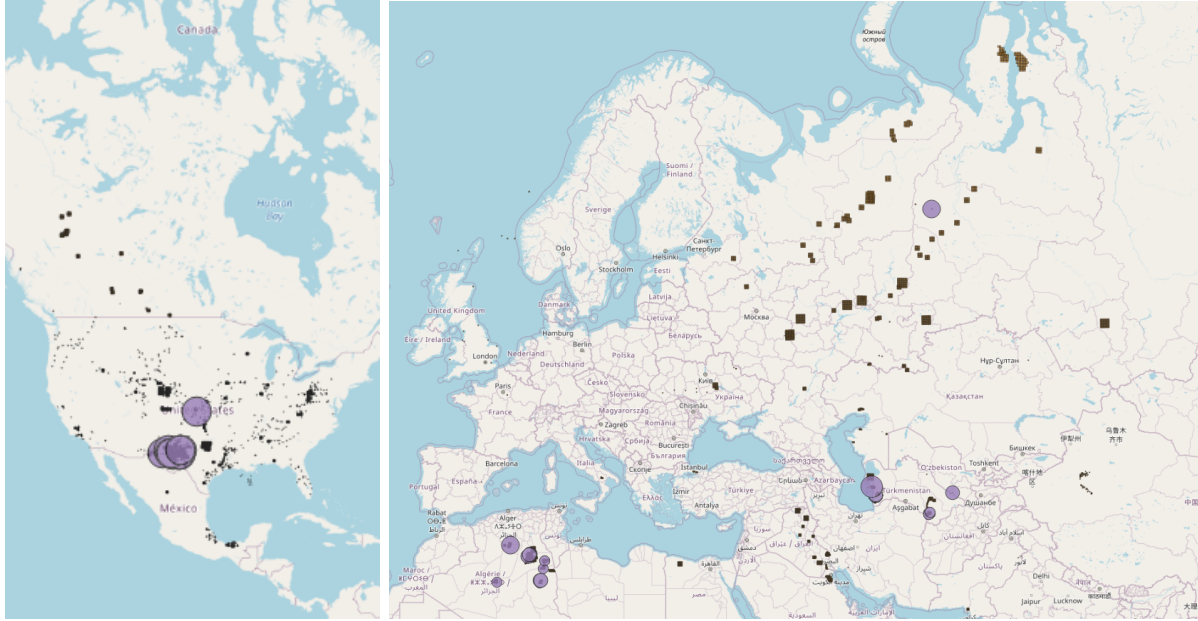


Figure 3: Illustration of the processed tiles and detected emissions. The quantified emission rate are illustrated by the circle diameters while the black squares represent the processed tiles. Figure best seen zoomed.

Table 2: Distribution by country of the detected emissions during the period of 43 months going from November 2017 to June 2021.

Country	Number of events
Algeria (DZA)	376
Turkmenistan (TKM)	325
United States (USA)	58
Uzbekistan (UZB)	27
Russian Federation (RUS)	5
Iraq (IRQ)	1
Kazakhstan (KAZ)	1

slope and complete the range for medium scale events, bridging the gap in emission rates between small sources ( $0.1 \text{ t}_{\text{CH}_4}/\text{hr}$  to  $10 \text{ t}_{\text{CH}_4}/\text{hr}$ ) captured by airborne campaigns and the ultra-emitters ( $> 25 \text{ t}_{\text{CH}_4}/\text{hr}$ ) detected by, for example, *Sentinel-5P*. This shows that at a global scale large event observations seen by *Sentinel-2* and *Sentinel-5P* might be a good proxy indicator for smaller events unobserved by these two satellites (these events can however be observed by airborne campaigns).

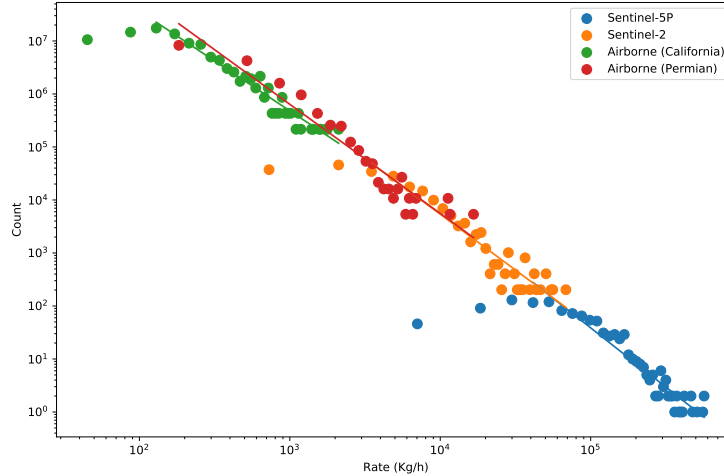


Figure 4: Power law plot of *Sentinel-5P* and *Sentinel-2* events, together with airborne campaigns over California<sup>2</sup> and the Permian.<sup>8</sup> Counts are scaled to match in common detection zones. Since data is consistent across the different sources used for the study, this shows that at a global scale large event observation might be a good proxy indicator for smaller but unobserved events.

## Per country analysis using *Sentinel-2* and *Sentinel-5P*

We analyzed the previous data on a per-country basis. We considered only measurements from *Sentinel-5P* and *Sentinel-2* and studied the detections in Algeria, Turkmenistan, and United States. This analysis is shown in Fig. 5. Out of the three countries studied here, Algeria shows lower magnitudes in terms of CH<sub>4</sub> emissions while Turkmenistan is the largest. However, we note that both countries follow a similar power law model. The United States suggest an intermediate level of emissions and a slightly different power law model. This country-based analysis confirms the coherence of *Sentinel-2* and *Sentinel-5P* data. Indeed, the slopes for both Algeria and Turkmenistan agree for both satellites despite spatially disconnected sampling and different emission rates. The case of the US is slightly more complicated to analyze. In practice, the regions studied by both satellites are different. The *Sentinel-2* measurements cover primarily the Permian basin while the *Sentinel-5P* ones cover the rest of the US. In both cases, the US is located in between Algeria and Turkmenistan.

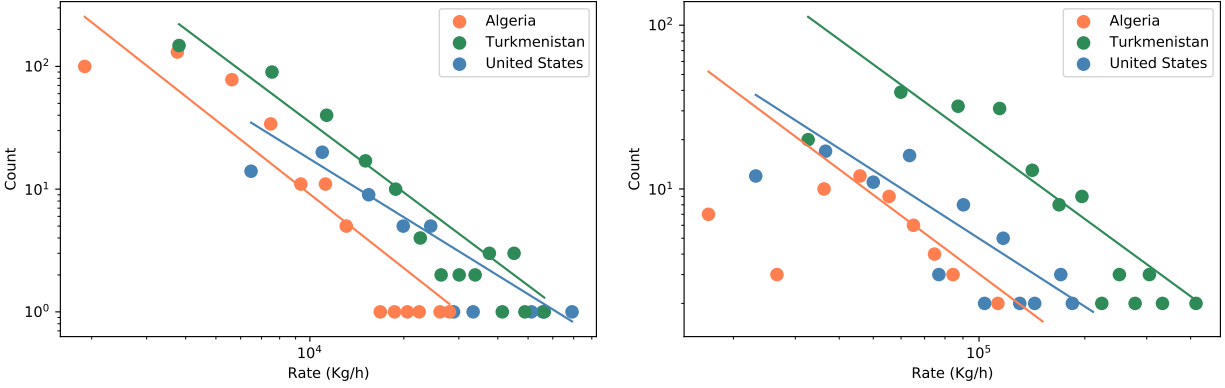


Figure 5: Power law by country from *Sentinel-2* (left) and *Sentinel-5P* (right) measurements. Out of the three countries studied, Algeria is doing the best in terms of CH<sub>4</sub> emissions while Turkmenistan is doing the worst, with the US in between.

## The September 2020 Permian incident

We also applied the same methodology to estimate emission rates during an incident in the Permian basin. This incident occurred during the summer of 2020<sup>1</sup> and lasted about two months. Several observations from *Sentinel-2*, *Landsat-8*, *Sentinel-5P* and from an airborne hyperspectral campaign were collected.

While we used the principle presented in Appendix A for *Landsat-8* and *Sentinel-2* imagery, *Sentinel-5P* measurements were derived from the methane concentrations provided by the L2 methane product. Nevertheless, we estimated a background methane concentration, by computing the median methane concentration neighboring a plume, that we then removed so that only the excess methane was measured. The airborne hyperspectral measurements were obtained in September 2020 (towards the end of the event) with Scientific Aviation flights and are provided by the PermianMap project (Operator Performance Dashboard<sup>2</sup>).

Fig. 6 shows the estimated emission rates from the mentioned sources. As we can see, the emission measurements of the airborne campaign and all those obtained after September 15<sup>th</sup> 2020 are all close and consistent with each other up until the last two EDF measurements.

<sup>1</sup>Estimated latitude and longitude of the source: (31.7335, -102.0421).

<sup>2</sup>Data from U. Arizona, NASA-JPL, and EDF provided via the PermianMap project by EDF (<https://data.permianmap.org/pages/operators>). Users are bound by the Terms of Use of this data.

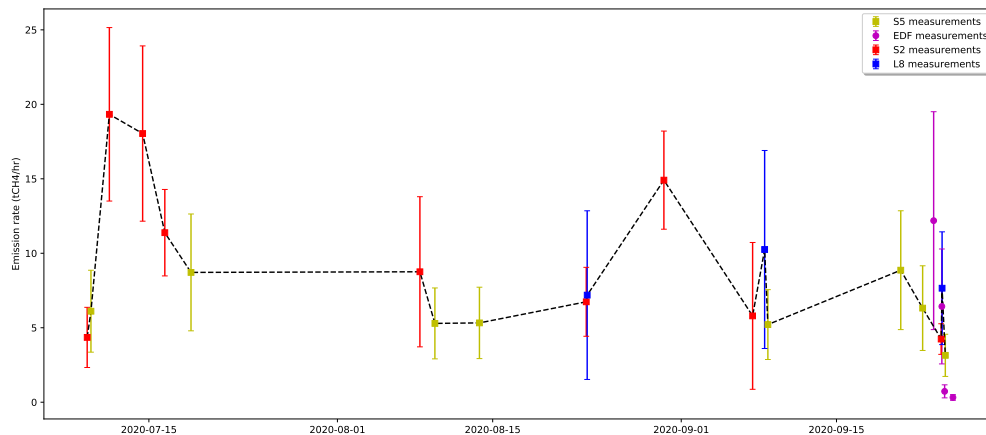


Figure 6: Emission rates measured during an incident in the Permian basin occurred during the summer of 2020 (estimated latitude and longitude: 31.7335, -102.0421). The plot combines estimates obtained from *Sentinel-2*, *Landsat-8*, *Sentinel-5P* and from Scientific Aviation flights. All of these estimates are consistent across sources and show that the emission started more than two months earlier than it was initially reported by the EDF campaign.

Yet, the analysis of the time series leads to conclude that the event had started two months prior to the aircraft campaign, thus increasing significantly the total amount of  $\text{CH}_4$  released. Note that the measurements as well as the estimated confidence intervals are consistent. In Fig. 7 we show the plumes observed at the 12 dates where *Sentinel-2* and *Landsat-8* images were available. Since no emissions were detected before July 9<sup>th</sup> 2020, these measurements enable a full description of the event from start to end and lead to estimate (by extrapolating each detected plume) a grand total of  $16,537 \pm 7,146$  tons of methane emitted during this event.

## Conclusions

Using our detection and quantification framework with *Sentinel-2* imagery, we were able to detect and monitor about 7,000 geographical sites with oil and gas infrastructure over many different countries. We detected and quantified more than 800 methane plumes across a period of 43 months.

We then used this data to complete the power law presented by Lauvaux *et al.*<sup>15</sup> This

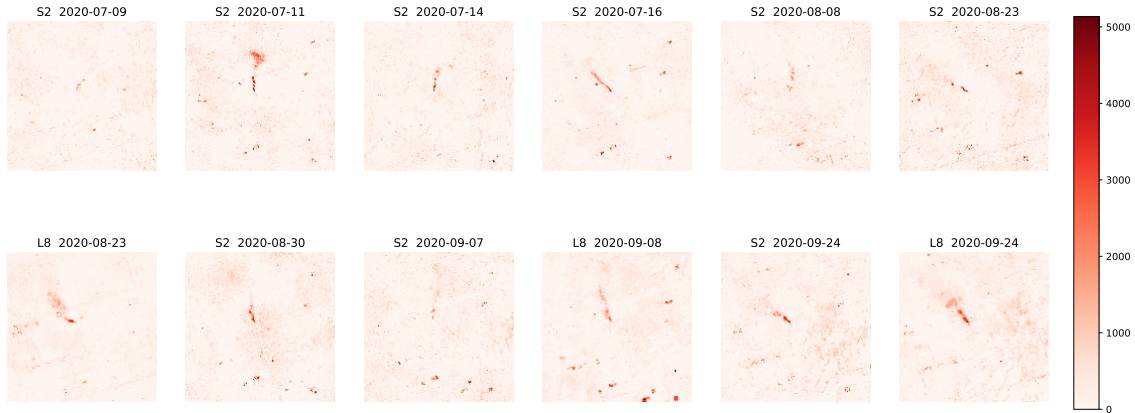


Figure 7: Illustration of the plumes (in ppb) observed using *Sentinel-2* and *Landsat-8* imagery during the incident in the Permian basin occurred during the summer of 2020 (estimated latitude and longitude: 31.7335, -102.0421) studied in Fig. 6. The source of the emission is located at the center of the images.

power law was initially made using only *Sentinel-5P*, only good for ultra-emitters ( $> 25$   $t_{\text{CH}_4}/\text{hr}$ ), and airborne campaigns, with limited spatial and temporal coverage. By involving *Sentinel-2*, we completed the picture by adding a large number of mid-scale detections. Since data are coherent across data sources, our study shows that global-scale ultra-emitters might be a good proxy indicator for smaller but unobserved events. We also looked at the behavior for different countries and across time. We were able to show that Algeria shows lower emission rates compared to Turkmenistan, with the US in between.

Finally, we verified the methodology on a specific incident in the Permian in September 2020. We combined observations from *Sentinel-2*, *Sentinel-5P* and *Landsat-8* and compared them to the results of an airborne campaign. Once again, the observations from the different data sources are coherent and show that the emission started more than two months prior to the airborne campaign. The estimated confidence intervals, between 1  $t_{\text{CH}_4}/\text{hr}$  and 6  $t_{\text{CH}_4}/\text{hr}$ , are also consistent between *Sentinel-2* and *Landsat-8*.

The next step is to make the entire framework completely automatic. Indeed, because we are currently relying on manual annotation to achieve the performance presented in this paper, we are limited to monitoring specific sites such as oil and gas infrastructures. Having a completely automatic pipeline would enable a global monitoring at high spatial resolution,

including attribution to specific facilities and activities in agricultural and waste sectors.

## Acknowledgement

The authors thank Omar Dhobb from Kayrros for his encouragement and support. Work partly financed by Office of Naval research grant N00014-17-1-2552, DGA Astrid project “Filmer la Terre” n° ANR-17-ASTR-0013-01, and MENRT. T. Lauvaux was supported by the French research program “Make Our Planet Great Again” (CNRS, project CIU-DAD). Alexandre d’Aspremont is at CNRS & département d’informatique, École normale supérieure, UMR CNRS 8548, 45 rue d’Ulm 75005 Paris, France, INRIA and PSL Research University, and would like to acknowledge support from the *ML and Optimisation* joint research initiative with the *fonds AXA pour la recherche* and Kamet Ventures, a Google focused award, as well as funding by the French government under management of Agence Nationale de la Recherche as part of the “Investissements d’avenir” program, reference ANR-19-P3IA-0001 (PRAIRIE 3IA Institute).

## Appendix A: Principles for methane detection and quantification with multi-spectral satellite imagery

When light traverses a gas, its intensity can be attenuated on certain wavelengths. Using this property, it is possible to detect the presence of a specific gas when its attenuation properties are known, and to derive a quantification of the concentration of this gas. In this paper, we apply this concept to methane detection using multi-spectral satellite imagery. We focus on the detection and quantification of isolated excess concentrations of methane in the atmosphere, also referred as anomalies. These phenomena are often due to emissions in oil and gas infrastructures. Since methane absorbs light in the SWIR part of the spectrum, it is possible to use satellites such as *Sentinel-2* (see Fig. 8) or *Landsat-8* (see Fig. 9) that

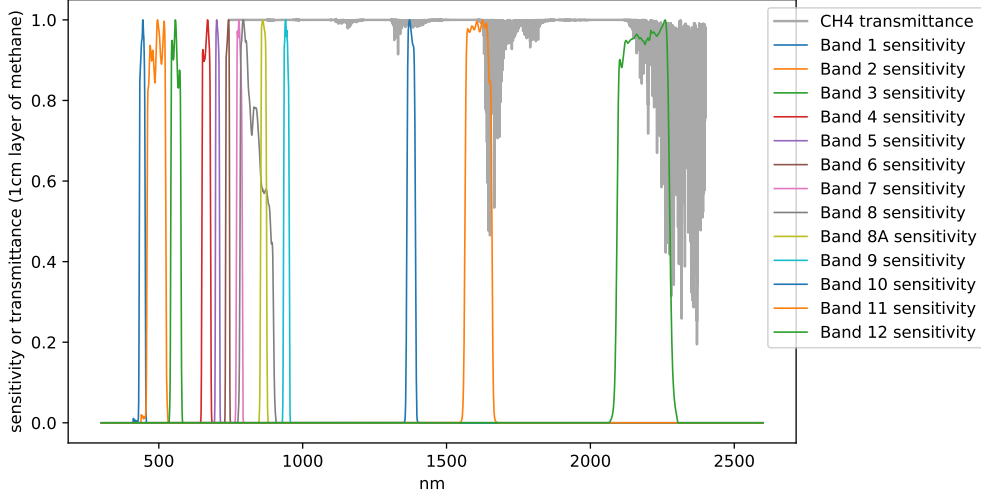


Figure 8: Methane transmittance spectrum and *Sentinel-2 A* spectral sensitivity for all its bands. Ignoring the cirrus band B10 that is not suitable for monitoring applications, only bands B11 (1568-1659 nm) and B12 (2114-2289 nm) are impacted by the presence of methane in the atmosphere. The other bands are not impacted.

provide a good spatial resolution, a low revisit time and a low acquisition cost.

We use a simple absorption model to characterize the attenuation due to the presence of methane. The Beer-Lambert law states that for a light source with intensity  $I_0$  and a wavelength  $\lambda$

$$I = I_0 e^{-\sum_{i=0}^N A_i(\lambda) l_i}, \quad (1)$$

where the light goes through  $N$  gases defined by their absorption  $A_i(\lambda)$  and equivalent optical path length  $l_i$  defined as the product of the actual optical path and the concentration of the  $i^{\text{th}}$  gas. In our case, the  $N$  gases correspond to the atmosphere and  $I_0$  is the sunlight in the SWIR spectrum. We can also reasonably assume  $I_0$  to be constant for all wavelengths  $\lambda$  of the SWIR spectrum. Taking into account that the sensor of a satellite integrates over a band of wavelengths described by a sensitivity function  $s$ , the intensity of the light seen by a space-borne sensor becomes

$$I = I_0 \int s(\lambda) \alpha(\lambda) e^{-\gamma \sum_{i=0}^N A_i(\lambda) l_i} d\lambda, \quad (2)$$

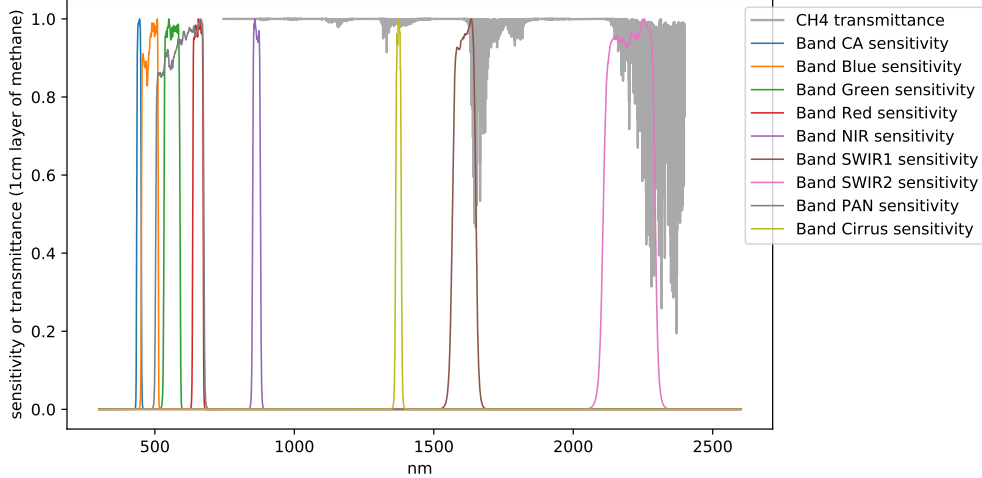


Figure 9: Methane transmittance spectrum and *Landsat-8* spectral sensitivity for all its bands. Similarly to *Sentinel-2*, the two SWIR bands SWIR1 and SWIR2 can be used for methane detection and quantification.

where the two passes through the atmosphere are taken into account in  $\gamma$  (which is a function of both the sun azimuth angle and the satellite view angle). The reflection coefficient of the ground is represented in the formula by the surface albedo  $\alpha(\lambda)$ . See Fig. 10.

In the presence of a methane emission, characterized by  $l_{leak}$ , the intensity of the light seen by the sensors becomes

$$I_{leak} = I_0 \int s(\lambda) \alpha(\lambda) e^{-\gamma \sum_{i=0}^N A_i(\lambda) l_i} e^{-\gamma A_{CH_4}(\lambda) l_{leak}} d\lambda. \quad (3)$$

Supposing that we have both the exact same observation with and without a methane emission, it becomes very easy to detect the emission. Indeed  $I_{leak} < I$  everywhere  $l_{leak}$  is non zero. The problem is that the observation without methane, also called background observation, is never available in practice. Therefore, a reference observation without methane is needed in order to distinguish an attenuation due to the presence of methane from a difference in the surface albedo.

When we assume that methane emissions are anomalous events, it is to be expected that most observations in a time series should not contain excess methane. So, if we suppose that the surface albedo is rather stable in time, the time series can be used to estimate a

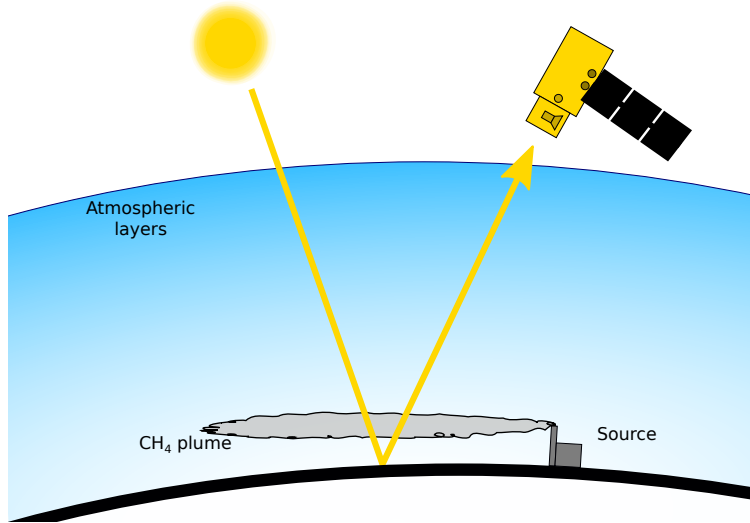


Figure 10: Atmosphere observation model. The on board sensor sees the light coming from the sun after reflection on Earth. Its intensity has dimmed due to the atmosphere and the reflection process. The dimming is also impacted by the presence of a methane plume.

methane free background model that can be compared with the current observation. Here, we compute the background for a given date as its linear regression over the previous dates. If we denote by  $I_t$  the observation at time  $t$ , then the regression computes the optimal weights  $w_i$  that solve

$$\min_{\{w_i\}} \left\| I_t - \sum_{i=0}^{t-1} w_i I_i \right\|^2. \quad (4)$$

Then the background is obtained as the linear combination  $\sum_{i=0}^{t-1} w_i I_i$ . To further improve the background subtraction we combine this estimation with a band ratio that exploits the correlation between SWIR bands, similarly to the *multiple-band single-pass* (MBSP) from Varon *et al.*<sup>19</sup>

Quantifying a emission is also an important part of monitoring. While the previous processing was presented for methane emission detection, it can also be used to quantify it. Supposing that both the signal with the emission  $I_{leak}$  and without emission  $I_{bg}$  are available (using for example the process presented previously), then

$$\frac{I_{leak}}{I_{bg}} \approx \frac{\int_{B12} s(\lambda) e^{-\gamma \sum_{i=0}^N A_i(\lambda) l_i} e^{-\gamma A_{CH4}(\lambda) l_{leak}} d\lambda}{\int_{B12} s(\lambda) e^{-\gamma \sum_{i=0}^N A_i(\lambda) l_i} d\lambda}. \quad (5)$$

Since  $\gamma$  is known for each acquisition, this ratio only depends on the atmosphere composition. Therefore, for a fixed atmosphere composition, it is possible to estimate the value of  $l_{leak}$  as the solution of a simple optimization problem

$$\arg \min_{l_{leak}} \left\| \frac{I_{leak}}{I_{bg}} - \frac{\int_{B12} s(\lambda) e^{-\gamma \sum_{i=0}^N A_i(\lambda) l_i} e^{-\gamma A_{CH_4}(\lambda) l_{leak}} d\lambda}{\int_{B12} s(\lambda) e^{-\gamma \sum_{i=0}^N A_i(\lambda) l_i} d\lambda} \right\|_2^2. \quad (6)$$

In practice, the atmosphere model can be well approximated with a simple “pure methane atmosphere”, *i.e.* an atmosphere that’s purely made of methane, instead of considering a complete atmosphere model. This quantification scheme can also be adapted when using band ratio.

## Appendix B: Practical methane emission tracking

We present in this Appendix the practical implementation of the detection and quantification principles mentioned in Appendix A. Namely, we first present the different preprocessing steps necessary for the pipeline to function. We provide more details about the background reconstruction process, the detection validation process and the quantification process. This practical pipeline is the one used to perform all the experiments presented in this paper. Fig. 11 illustrates the different steps of the proposed methodology for *Sentinel-2*; Fig. 12 illustrates the same steps but for *Landsat-8*.

### Preprocessing

From now on, we consider areas of interest (AOIs) of size approximately 10x10 km<sup>2</sup>. We found out that this size is well adapted to capture methane plumes created by emissions, while being large enough so that the reconstruction is not impacted too much by the presence of methane in the reference images. We collect L1C *Sentinel-2* timeseries corresponding to the AOIs, preferably considering timeseries longer than six months. We first co-register

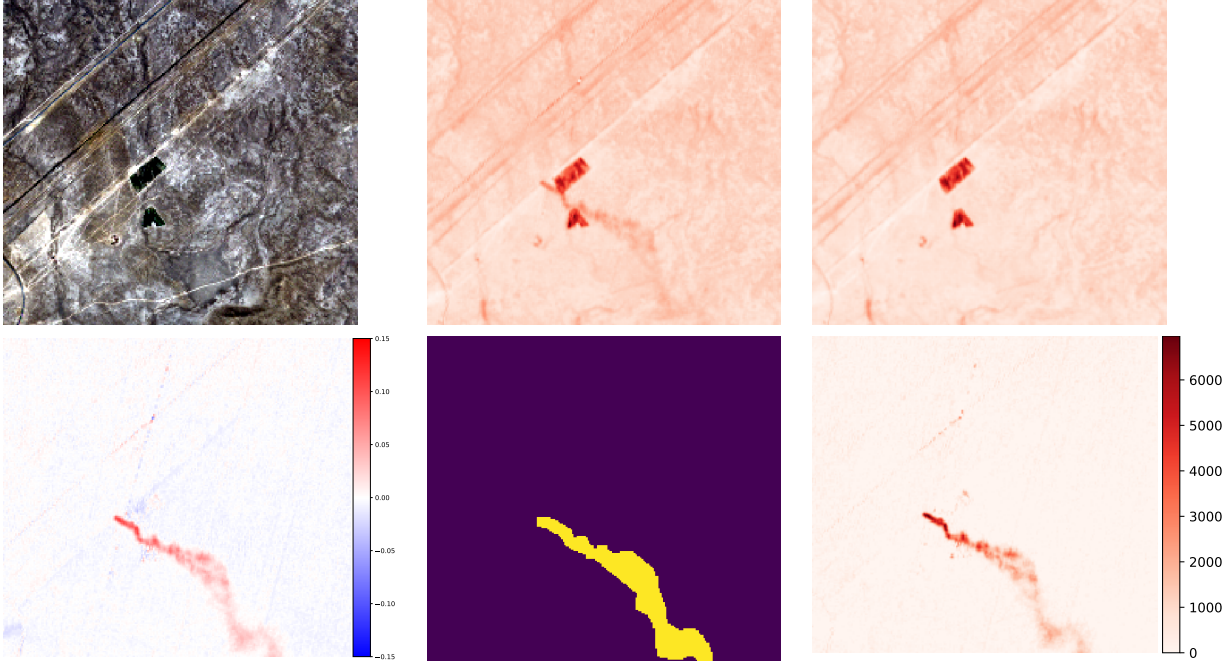


Figure 11: Visualization of each step of the detection and quantification pipeline. From left to right, top to bottom: the *Sentinel-2* image of the location (only the RGB channels are shown), the log band ratio corresponding to the image, the predicted background model, the residual showing the plume, the mask corresponding to the detected plume and the associated quantification in ppb.

all the images of a timeserie using the method by Hessel *et al.*<sup>21</sup> We also apply a cloud detection algorithm, such as the one proposed by Dagobert *et al.*,<sup>22</sup> to estimate the cloud cover. All images with a cloud coverage of more than 15% of the pixels from the image are discarded. Sentinel-2 images comprise 12 bands with spatial resolutions from 10m per pixel to 60m per pixel. The two bands of interest, namely band 11 and band 12, are both sampled at 20m per pixel therefore there is no need for resampling them. However, we have observed that these two bands are aliased. This is particularly important because we are computing ratios of these two bands and therefore this aliasing can create large artifacts during the processing (see Fig. 13). In order to avoid this problem we apply an anti-aliasing filter, namely a Gaussian filter, prior to any other processing. We also apply a log on the ratio. This limits the impact on the reconstruction of abnormal high values present in the SWIR bands, for example due to flaring, which are frequently found in the vicinity of oil

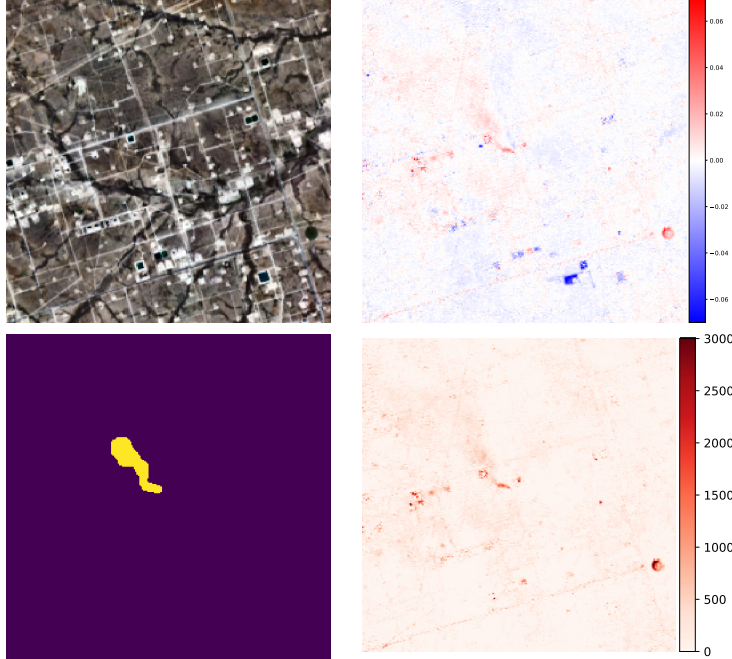


Figure 12: Visualization of each step of the detection and quantification pipeline. From left to right, top to bottom: the *Landsat-8* image of the location (only the RGB channels are shown), the log band ratio corresponding to the image, the predicted background model, the residual showing the plume, the mask corresponding to the detected plume and the associated quantification in ppb.

and gas facilities. As it will be seen in *Detection validation*, the other bands are still useful to validate a plume detection. This is why we resample all these bands to 20m per pixel so that comparison is easier.

## Background estimation

The core of the detection pipeline is the background estimation process. For that we split each time-series of log band ratios computed above in a sliding window of size  $T = 30$  dates. For each date in the window, we compute its linear projection on the past  $T - 1$  images. Using the estimated background, we define a residual that corresponds to the difference between the input data and the prediction. Fig. 14 illustrates the impact of the size of the sliding window  $T$  on the background estimation. A longer time series improves the SNR of the extracted plume, thus fostering its detection. Note that by projecting on a time series

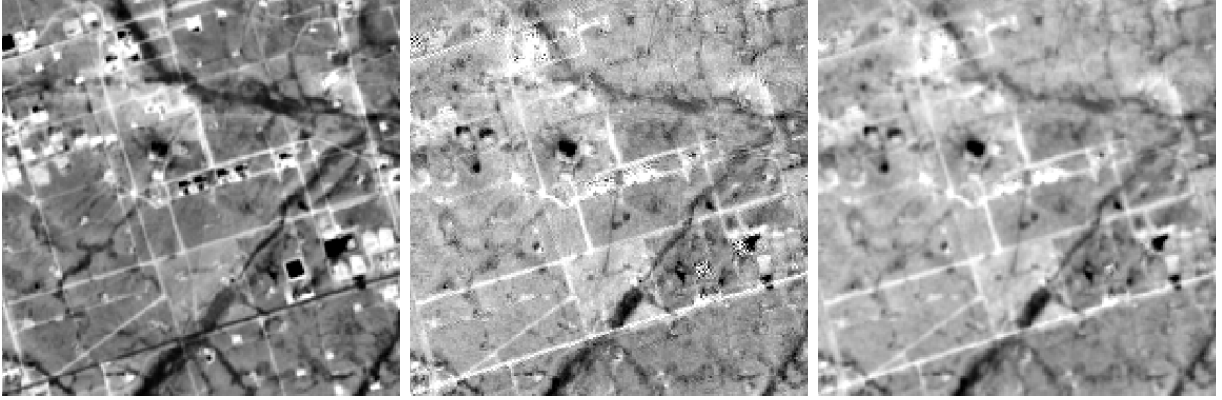


Figure 13: From left to right: Band 12, ratio between B12 and B11 without filtering and ratio between B12 and B11 with filtering. *Sentinel-2* images are aliased and therefore should be preprocessed before computing the ratio. The artifacts due to aliasing would impact the processing otherwise. Figure best seen zoomed.

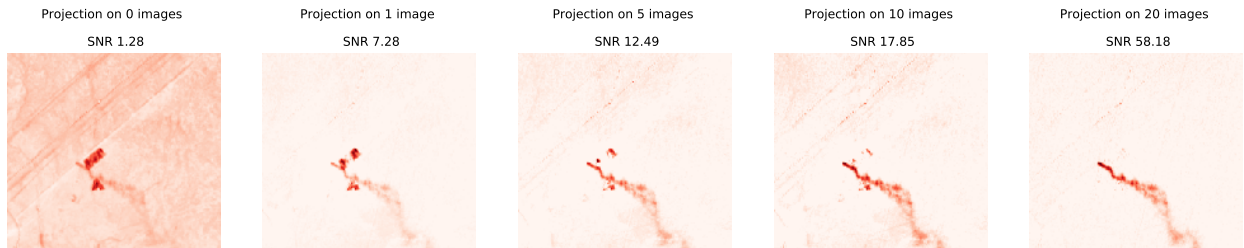


Figure 14: Impact of the size of the sliding window  $T$  on the background estimation. A longer time series improves the SNR of the extracted plume thus helps its detection.

there is no need to manually choose a reference date as background.<sup>19</sup>

Similarly to how flaring could impact the background estimation, new (or disappearing) large structure can also lead to errors in the quantification. To limit the impact of outliers, robust estimation methods such as Huber regression<sup>23</sup> or the iteratively reweighted least square algorithm<sup>24</sup> can be used. We found out that in our case such robust regression methods are quite slow. For this reason, we use an approximate two-steps estimation method that is good enough for this application. A first estimation is done using a linear projection as presented previously. Then the 5% of pixels with the worst estimation are discarded. The remaining pixels are then used to perform a second linear projection, this time without the outliers. The coefficients estimated with the second linear projection are used to perform the final estimation. We argue that even if pixels containing methane are initially discarded,

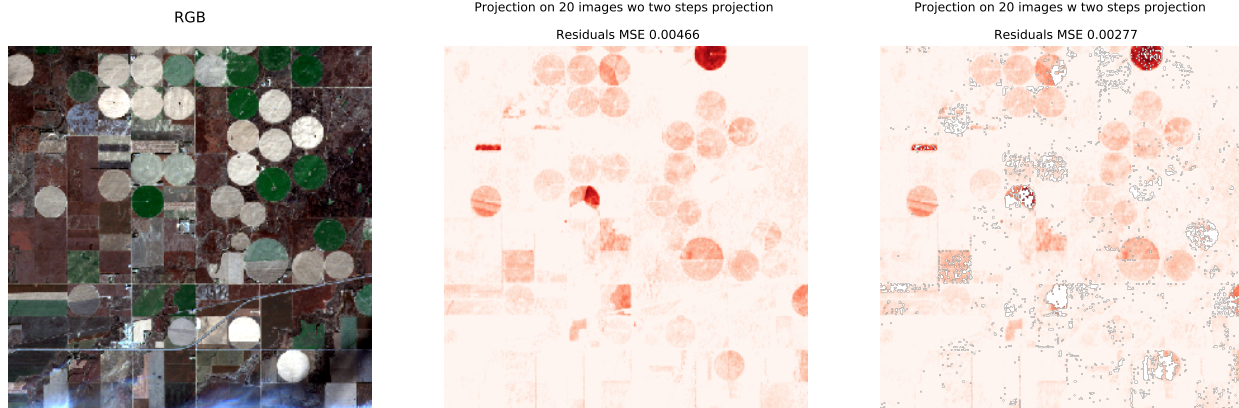


Figure 15: Improvement of background estimation when using a two-steps estimation. Left to right: The RGB image of the scene, the background estimated using a single step, the background estimated using two steps. Using two steps allows to have a much smaller MSE than a single step estimation (with the outliers set to zero). The MSE has been estimated on the same pixels (*i.e.* without the outliers) for both images.

this is not a problem because methane should, by definition, not impact the background prediction. Fig. 15 shows a case in which this procedure allows to refine the background reconstruction. The reconstruction error of the background is almost twice as small when using a two step estimation.

Despite removing outliers, the two-stage approach cannot deal with time series containing large zones with changing albedo. This is the case for the crop fields seen in Fig. 16, for which a spatially adaptive processing must be adopted. The objective is to bring non linearity to the projection by performing one projection for each zone of similar albedo. An albedo map is computed by clustering the pixels of our images with four different features: the temporal standard deviation and mean of the band absorbing median, the  $x$  and  $y$  position of the pixel in the image. The clustering is done using a Gaussian mixture model, and the optimal number of clusters is fixed with the post analysis of the Bayesian information criterion of the clustering. This methodology being more computationally intensive is performed only on regions with a high albedo variance.

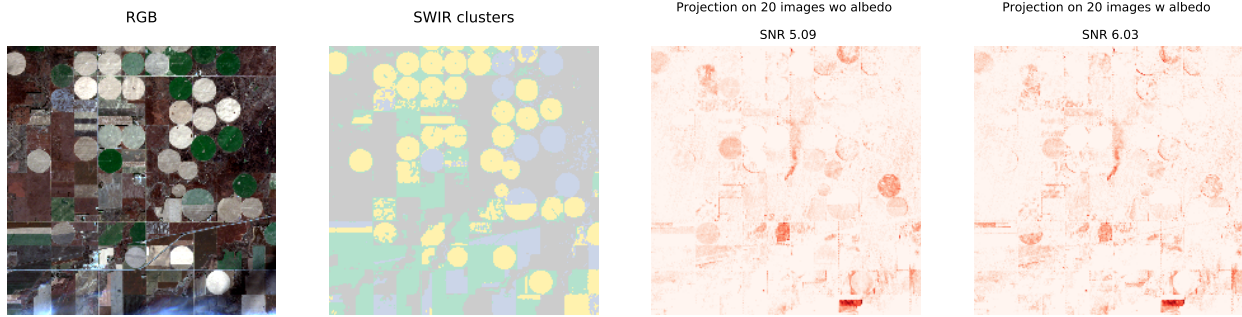


Figure 16: Improvement of background estimation when using clustering. Left to right: The RGB image of the scene, the different clusters estimated from the albedo, the background estimated without the clusters, the background estimated with the clusters. Using a clustering step during the background estimation increases the SNR of the methane plume with respect to the background.

## Detection validation

While we would like to have a completely automatic detection process, directly detecting on the residuals computed in *Background estimation* yielded too many false detections. This is why we added an extra step where all detections are done and verified manually. In particular, a mask corresponding to the shape of the potential plume is first manually annotated. We then compare the content of the annotated region to the content of the same region but in the other bands. If the potential plume is indeed a true methane plume, then it should not be correlated to the content of the bands that are not impacted by the presence of methane. In particular, a similar shape should not be found in these other bands. Some surfaces, for example snow, have a higher reflectance in B11 than B12. This causes a contrast inversion and a dimming-like phenomenon when looking at the band ratio. Because of that, it is possible that potential plumes appear in the band ratio even though they do not correspond to an actual dimming in B12. The last validation step checks that the detection corresponds indeed to a dimming in B12.

## Source quantification

Once the mask of the plume is available, we quantify the emission rate corresponding to the source of the plume. The first step is to quantify the equivalent amount of methane  $l_{CH_4}$  per pixel that corresponds to the extra methane attributed to the source. For that, we adapt the quantification model presented in Eq. 6 so as to take into account the extra log preprocessing as well as the band ratio. This leads to an extra methane  $\Delta\Omega(p)$  for the pixel  $p$  corresponding to

$$\Delta\Omega(p) = \arg \min_{l_{eak}} \left\| R(p) - \log \left( \frac{\int_{B12} s(\lambda) e^{-\gamma A_{CH_4}(\lambda)(l_{atm} + l_{eak})} d\lambda}{\int_{B12} s(\lambda) e^{-\gamma A_{CH_4}(\lambda)l_{atm}} d\lambda} \frac{\int_{B11} s(\lambda) e^{-\gamma A_{CH_4}(\lambda)l_{atm}} d\lambda}{\int_{B11} s(\lambda) e^{-\gamma A_{CH_4}(\lambda)(l_{atm} + l_{eak})} d\lambda} \right) \right\|_2^2, \quad (7)$$

with  $R(p)$  the estimated residual at pixel  $p$  and  $l_{atm}$  the amount of methane naturally present in the atmosphere. We define  $l_{atm}$  such that it corresponds to a residual background of 1800ppb of methane. To estimate  $A_{CH_4}$ , we use the HITRAN database.<sup>25</sup> We also use the sensitivity  $s$  of *Sentinel-2 A*, respectively *Sentinel-2 B*, calibrated in laboratory provided by ESA<sup>3</sup>. The optimization is done using the downhill simplex algorithm.

Once each pixel of the plume has been quantified, we estimate the source emission rate using the integrated mass enhancement (IME) method.<sup>26</sup> The IME method relates the source rate  $Q$  to the total detected plume mass by

$$Q = A \frac{U_{eff}}{L} \sum_{pin\mathcal{M}} \Delta\Omega(p), \quad (8)$$

where  $U_{eff}$  corresponds to the effective wind speed,  $L$  the plume length,  $\mathcal{M}$  the mask of the plume,  $A$  the area covered by a pixel (in this case  $A = 400\text{m}^2$ ). We use wind data collected from the ECMWF-ERA5 reanalysis product from the Copernicus Climate Change Service.<sup>20</sup> Varon *et al.*<sup>26</sup> showed that  $U_{eff}$  can be related to the local wind speed at 10m  $U_{10}$  therefore we select the wind product at 10m above ground level and at the closest time before the sensing time for each estimation. The source origin is selected manually using jointly the

<sup>3</sup><https://sentinels.copernicus.eu/web/sentinel/technical-guides/sentinel-2-msi/performance>

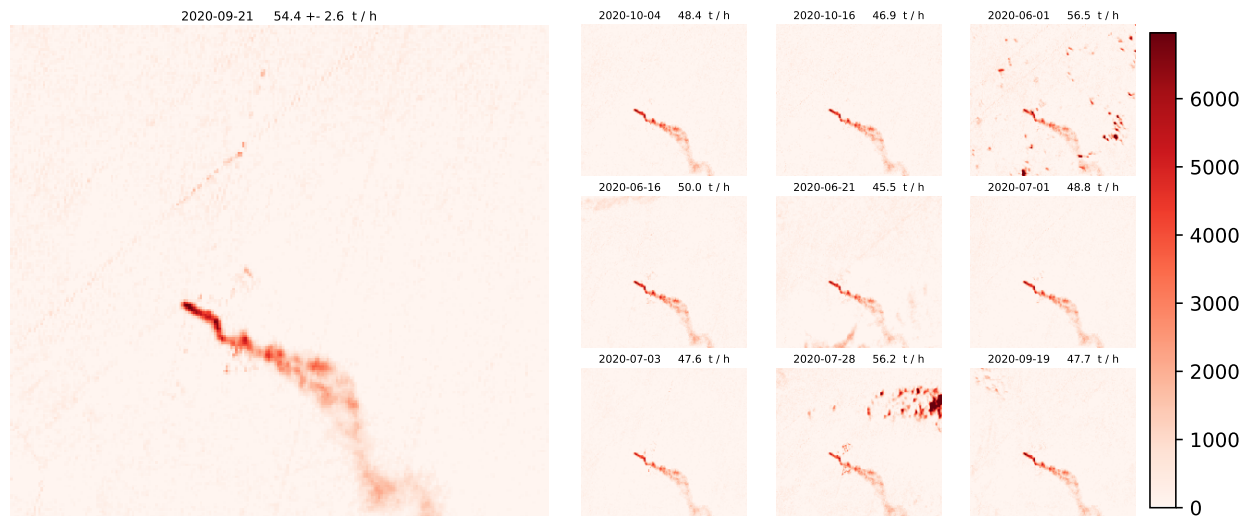


Figure 17: The uncertainty of the plume on the left is estimated by simulating the same plume in other images of the timeseries. Each estimated plume (in ppb) as well as their predicted emission rate are shown on the right.

wind data and the plume shape.

## Quantification uncertainty estimation

Different factors can contribute to quantification errors in the proposed method. We focus here on the uncertainty induced by the proposed background estimation method by providing a per-scene uncertainty estimation.

Fluctuations in the albedo and atmospheric conditions might be wrongly quantified as excess of methane. The idea is to estimate the quantification errors due to these fluctuations by simulating the same methane plume in other images of the time series: From each new simulated image the quantification pipeline is run again and a new emission rate is estimated. The uncertainty is then obtained as the standard deviation of the emission rates estimated with the simulated images. Fig. 17 illustrates the concentrations obtained by applying this procedure on different images of the time series.

## References

- (1) Brandt, A. R.; Heath, G.; Kort, E.; O’Sullivan, F.; Pétron, G.; Jordaan, S. M.; Tans, P.; Wilcox, J.; Gopstein, A.; Arent, D., et al. Methane leaks from North American natural gas systems. *Science* **2014**, *343*, 733–735.
- (2) Duren, R. M.; Thorpe, A. K.; Foster, K. T.; Rafiq, T.; Hopkins, F. M.; Yadav, V.; Bue, B. D.; Thompson, D. R.; Conley, S.; Colombi, N. K., et al. California’s methane super-emitters. *Nature* **2019**, *575*, 180–184.
- (3) McKeever, J.; Jarvis, D.; Strupler, M.; Gains, D.; Tarrant, E.; Varon, D. J.; Maasackers, J. D.; Pandey, S.; Houweling, S.; Aben, I., et al. Detection and Imaging of Methane Emissions Plumes from Oil and Gas Facilities with GHGSat-D. AGU Fall Meeting Abstracts. 2019; pp GC51M–0962.
- (4) Varon, D.; McKeever, J.; Jarvis, D.; Maasackers, J.; Pandey, S.; Houweling, S.; Aben, I.; Scarpelli, T.; Jacob, D. Satellite discovery of anomalously large methane point sources from oil/gas production. *Geophysical Research Letters* **2019**, *46*, 13507–13516.
- (5) Zhang, Y.; Gautam, R.; Pandey, S.; Omara, M.; Maasackers, J. D.; Sadavarte, P.; Lyon, D.; Nesser, H.; Sulprizio, M. P.; Varon, D. J., et al. Quantifying methane emissions from the largest oil-producing basin in the United States from space. *Science Advances* **2020**, *6*, eaaz5120.
- (6) Guha, A.; Newman, S.; Fairley, D.; Dinh, T. M.; Duca, L.; Conley, S. C.; Smith, M. L.; Thorpe, A. K.; Duren, R. M.; Cusworth, D. H., et al. Assessment of Regional Methane Emission Inventories through Airborne Quantification in the San Francisco Bay Area. *Environmental Science & Technology* **2020**, *54*, 9254–9264.
- (7) Irakulis-Loitxate, I.; Guanter, L.; Liu, Y.-N.; Varon, D. J.; Maasackers, J. D.; Zhang, Y.; Chulakadabba, A.; Wofsy, S. C.; Thorpe, A. K.; Duren, R. M., et al.

- Satellite-based survey of extreme methane emissions in the Permian basin. *Science Advances* **2021**, *7*, eabf4507.
- (8) Cusworth, D. H.; Duren, R. M.; Thorpe, A. K.; Olson-Duvall, W.; Heckler, J.; Chapman, J. W.; Eastwood, M. L.; Helmlinger, M. C.; Green, R. O.; Asner, G. P., et al. Intermittency of Large Methane Emitters in the Permian Basin. *Environmental Science & Technology Letters* **2021**,
- (9) Intergovernmental Panel on Climate Change,, Ed. *Climate Change 2013 - The Physical Science Basis*; Cambridge University Press: Cambridge, 2013; pp 659–740.
- (10) Lyon, D. R.; Alvarez, R. A.; Zavala-Araiza, D.; Brandt, A. R.; Jackson, R. B.; Hamburg, S. P. Aerial surveys of elevated hydrocarbon emissions from oil and gas production sites. *Environmental science & technology* **2016**, *50*, 4877–4886.
- (11) Veefkind, J.; Aben, I.; McMullan, K.; Förster, H.; De Vries, J.; Otter, G.; Claas, J.; Eskes, H.; De Haan, J.; Kleipool, Q., et al. TROPOMI on the ESA Sentinel-5 Precursor: A GMES mission for global observations of the atmospheric composition for climate, air quality and ozone layer applications. *Remote sensing of environment* **2012**, *120*, 70–83.
- (12) Pandey, S.; Gautam, R.; Houweling, S.; Van Der Gon, H. D.; Sadavarte, P.; Borsdorff, T.; Hasekamp, O.; Landgraf, J.; Tol, P.; Van Kempen, T., et al. Satellite observations reveal extreme methane leakage from a natural gas well blowout. *Proceedings of the National Academy of Sciences* **2019**, *116*, 26376–26381.
- (13) Schneising, O.; Buchwitz, M.; Reuter, M.; Vanselow, S.; Bovensmann, H.; Burrows, J. P. Remote sensing of methane leakage from natural gas and petroleum systems revisited. *Atmospheric Chemistry and Physics* **2020**, *20*, 9169–9182.
- (14) Barré, J.; Aben, I.; Agustí-Panareda, A.; Balsamo, G.; Bousserez, N.; Dueben, P.; Engelen, R.; Inness, A.; Lorente, A.; McNorton, J., et al. Systematic detection of local

- CH 4 anomalies by combining satellite measurements with high-resolution forecasts. *Atmospheric Chemistry and Physics* **2021**, *21*, 5117–5136.
- (15) Lauvaux, T.; Giron, C.; Mazzolini, M.; d’Aspremont, A.; Duren, R.; Cusworth, D.; Shindell, D.; Ciais, P. Global Assessment of Oil and Gas Methane Ultra-Emitters. *arXiv preprint arXiv:2105.06387* **2021**,
- (16) Cusworth, D. H.; Jacob, D. J.; Varon, D. J.; Chan Miller, C.; Liu, X.; Chance, K.; Thorpe, A. K.; Duren, R. M.; Miller, C. E.; Thompson, D. R., et al. Potential of next-generation imaging spectrometers to detect and quantify methane point sources from space. *Atmospheric Measurement Techniques* **2019**, *12*, 5655–5668.
- (17) McKeever, J.; Deglint, H.; Gains, D.; Jervis, D.; MacLean, J.-P.; Ramier, A.; Shaw, W.; Strupler, M.; Tarrant, E.; Varon, D.; Young, D. First methane sensing results from GHGSat’s commercial constellation. 2021.
- (18) Scafutto, R. D. M.; van der Werff, H.; Bakker, W. H.; van der Meer, F.; de Souza Filho, C. R. An evaluation of airborne SWIR imaging spectrometers for CH<sub>4</sub> mapping: Implications of band positioning, spectral sampling and noise. *International Journal of Applied Earth Observation and Geoinformation* **2021**, *94*, 102233.
- (19) Varon, D. J.; Jervis, D.; McKeever, J.; Spence, I.; Gains, D.; Jacob, D. J. High-frequency monitoring of anomalous methane point sources with multispectral Sentinel-2 satellite observations. *Atmospheric Measurement Techniques* **2021**, *14*, 2771–2785.
- (20) ERA5: Fifth generation of ECMWF atmospheric reanalyses of the global climate. Copernicus Climate Change Service (C3S). <https://cds.climate.copernicus.eu/cdsapp#!/home>, Accessed: 2021-07-01.
- (21) Hessel, C.; de Franchis, C.; Facciolo, G.; Morel, J.-M. A global registration method for satellite image series. IGARSS 2021 IEEE International Geoscience and Remote Sensing Symposium. 2021.

- (22) Dagobert, T.; Grompone von Gioi, R.; de Franchis, C.; Morel, J.-M.; Hessel, C. Cloud Detection by Luminance and Inter-band Parallax Analysis for Pushbroom Satellite Imagers. *Image Processing On Line* **2020**, *10*, 167–190, <https://doi.org/10.5201/ipol.2020.271>.
- (23) Huber, P. J. *Robust statistics*; John Wiley & Sons, 2004; Vol. 523.
- (24) Weiszfeld, E. Sur le point pour lequel la somme des distances de n points donnés est minimum. *Tohoku Mathematical Journal, First Series* **1937**, *43*, 355–386.
- (25) Gordon, I. E. et al. The HITRAN2016 molecular spectroscopic database. *Journal of Quantitative Spectroscopy and Radiative Transfer* **2017**,
- (26) Varon, D. J.; Jacob, D. J.; McKeever, J.; Jervis, D.; Durak, B. O.; Xia, Y.; Huang, Y. Quantifying methane point sources from fine-scale satellite observations of atmospheric methane plumes. *Atmospheric Measurement Techniques* **2018**, *11*, 5673–5686.